Core-Shell Colloidal Nanocomposites for Local Temperature Monitoring During Photothermal Heating

Veronica Zani,[a] Carlos Renero-Lecuna,[†,b,c,*] Dorleta Jimenez de Aberasturi,[b,d] Desirè di Silvio,[b] Safiyye Kavak,[e] Sara Bals,[e] Raffaella Signorini,[a] and Luis M. Liz-Marzán [b,c,d,f,*]

[a] Università degli Studi di Padova, Department of Chemical Sciences, via Marzolo 1, 35131 Padova, Italy.

[b] CIC biomaGUNE, Basque Research and Technology Alliance (BRTA), 20014 Donostia-San Sebastián, Spain.

[c] Biomedical Networking Center on Bioengineering, Biomaterials and Nanomedicine (CIBER-BBN), 20014 Donostia-San Sebastián, Spain.

[d] Ikerbasque, Basque Foundation for Science, 48009 Bilbao, Spain

[e] EMAT and NANOlab Center of Excellence, University of Antwerp, 2020 Antwerp, Belgium.

[f] Cinbio, University of Vigo, 36310 Vigo, Spain

*e-mail: llizmarzan@cicbiomagune.es; carlos.renero@uvigo.gal;

Keywords: nanothermometry, local temperature, nanocomposite, multi-modal, biological windows

Abstract

Determining temperature changes at the heating site to accurately control thermal treatments has been a major goal in the field of nanothermometry. In this study, we address the need to effectively monitor local temperature during the application of photothermal therapies, which is essential to prevent uncontrolled heating induced by nanoparticle sensitizers used in such treatments. For this purpose, we developed a synthetic protocol to produce a nanocomposite probe that allows local photothermal heating and simultaneous *in situ* optical nanothermometry, within the biological transparency windows. The nanocomposite material comprises gold nanorods for light-to-heat conversion and neodymium (Nd^{3+})-based nanoparticles for local temperature monitoring. An inert spacer made of mesoporous silica provides a core-shell structure and ensures uniform separation between both functionalities to prevent photoluminescence quenching. By using an 808 nm laser as the source for both heating and photoluminescence excitation, we demonstrate a direct correlation between local temperature and near infrared Nd^{3+} emission intensities, thereby providing precise local temperature monitoring. Different levels of local heating were studied by varying the incident laser power, resulting in a maximum temperature increase of 47 °C detected with the nanothermometers. Albeit presented here as a proof of concept, this concept can be translated to the design of materials for photothermal therapy.

Introduction

Temperature is a crucial parameter for living organisms because it is a determining factor in many biological processes, such as cell division, gene expression, enzymatic reactions, and changes in metabolic activity. Both temperature evaluation for disease detection and its application to purposely cause damage to harmful cells are of primary interest.[1] Localized thermal treatments can be used in combination with conventional therapies to minimize their side effects.[2,3] Among other treatments that exploit higher (irreversible injury treatments, above 48 °C) or lower (diathermia, up to 41 °C) temperature increments, hyperthermia has raised significant interest in the scientific community. Particular attention is paid toward cancer treatment because the temperature range of 41-48 °C appears to be ideal to cause cancer cell death.[4,5] Such localized therapies are enabled by using nanoparticles (nanoheaters) that can generate heat under various external stimuli, such as laser irradiation in the case of photothermal therapy (PTT) or an alternating magnetic field in magnetic hyperthermia.[6,7] The efficacy of PTT can be enhanced by increasing the penetration depth of the treatments, which requires the use of laser wavelengths in the near-IR (NIR) biological window (BW) spectral ranges, in which absorption and scattering by human tissue are reduced. The main BWs range from 650 to 980 nm (BW-I) and from 1000 to 1400 nm (BW-II).[8,9]

Widely used materials for application as nanoheaters are gold nanoparticles,[4] in particular those with anisotropic morphologies such as gold nanorods (AuNRs), which display a widely tunable longitudinal surface plasmon resonance (LSPR). By controlling the size and aspect ratio of AuNRs, the LSPR can be driven into the NIR, including the BW spectral ranges for PTT.[10–13]

To accomplish the task of local temperature monitoring, the invasiveness of the nanothermometry method should be minimized as much as possible. The use of optical probes with spectral features that depend on temperature is suitable for this purpose.[7–9] The optical response, *i.e*. the excitation and emission of nanothermometers, should also be tuned within the BWs.[8] There are numerous examples in the literature reporting temperature measurements by means of luminescent probes,[14–16] *e.g*. through the ratio between two emission intensities that correspond to thermally coupled electronic levels, with population densities that follow a Boltzmann distribution. Neodymium ions (Nd^{3+}), which absorb around 800 nm ($^4I_{9/2}\rightarrow{}^4F_{5/2}$, $^2H_{9/2}$) and emit in the NIR ($^4F_{3/2}\rightarrow{}^4I_{13/2}$, $^4F_{3/2}\rightarrow{}^4I_{11/2}$, $^4F_{3/2}\rightarrow{}^4I_{9/2}$), are particularly suitable for nanothermometry, by monitoring the intensity ratio between their intraband or interband emission lines.[17]

The use of optical nanothermometers is particularly relevant in the implementation of PTT, through real-time monitoring of local temperature changes and fine-tuning therapeutic parameters, so damage to surrounding healthy tissues can be minimized. This cannot be accomplished by conventional IR thermometry cameras because they provide surface temperature information, at the skin level, which differs significantly from the actual temperature within subcutaneous tumors, usually underestimating tumor temperature and collateral damage.[18,19] Additionally, thermal cameras have a spatial resolution in the millimeter range, which is insufficient for local temperature determination, especially during hyperthermia treatments, where temperature should be kept below 48 °C to avoid irreversible damage to healthy tissue. Therefore, the combination of luminescent nanothermometers with nanoheaters emerges as a solution to fine-tune the parameters used for photothermal therapy. Some studies have dealt with mixing nanoheaters and photoluminescent temperature probes, within the same colloidal dispersion (**Figure 1A**).[20] However, the use of separate nanoparticles for heat generation and temperature determination may result in an excessive and inhomogeneous spatial separation between nanoheaters and nanothermometers. As a result, the temperature readout is inevitably averaged over the irradiated sample volume, thus including contributions from all nanothermometers, not just those in proximity to nanoheaters.

Alternative strategies for measuring temperature in the vicinity of the heating nanoparticles include the use of nanoparticles featuring both heating and thermometry functionalities, or composite particles where nanoheaters and nanothermometers are bound to each other. The former strategy (**Figure 1B**) refers to nanoparticles such as Nd^{3+}:LaF_3, in which the thermal sensitivity of Nd^{3+} luminescence bands is exploited for nanothermometry while an increased Nd^{3+} content enhances their light-to-heat conversion efficiency.[21]

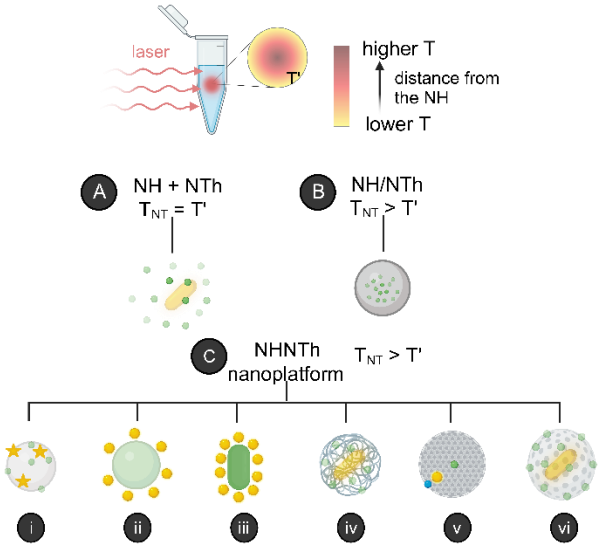

Figure 1. Schematic illustration of different configurations for combining nanoheaters (NH) and nanothermometers (NTh); the local temperature sensed by the nanothermometers (T_{NT}) may differ from the bulk solution temperature (T'): (A) mixing NH and NTh in the same colloidal dispersion;[20] (B) using the same nanomaterial for heating and thermometry, and (C) constructing multifunctional composites by: (i) attaching NTh and NH to a third material; (ii, iii) NTh shells of different shapes decorated with NHs; (iv) a temperature sensitive capsule embedding both NH and NTh; (v), a combination of different NTh in a hybrid core multi-shell particle, with two different temperature readings; and (vi) a NH in the center of a dielectric shell and NTh at a fixed distance (on the shell surface).

A third strategy involves the use of multi-component nanomaterials for simultaneous local heating and thermal sensing, such as those sketched in **Figure 1C**. Examples of this strategy include the use of hybrid nanostructures combining Au nanoparticles (nanostars in **Figure 1C(i)**) as photothermal agents with CaF_2:Nd^{3+},Y^{3+} nanoparticles as luminescent nanothermometers,[22] Au nano-shells decorated with upconverting nanoparticles of $NaGdF_4$ doped with Yb^{3+} and Er^{3+} ions (**Figure 1C(ii)**),[23] $(Gd,Yb,Er)_2O_3$ nanorods decorated with Au nanoparticles (**Figure 1C(iii)**),[24] either Au NRs and Nd^{3+}:LaF_3 nanoparticles embedded in a single poly(lactic-co-glycolic acid) (PLGA) capsule or coated in an inorganic capsule of $Y(V,P)O_4$:Eu^{3+} nanocrystals (**Figure 1C(iv)**).[25,26] In a further development, Lin *et al*.[27] combined upconverting nanoparticles, quantum dots and Au nanoparticles at different positions of mesoporous silica particles, thereby allowing two different temperature readings and distribution at the nanoscale (**Figure 1C(v)**).

Our approach comprises the synthesis of colloidal composites where the nanothermometers are placed at a fixed distance from a central nanoheater (**Figure 1C(vi)**). We hypothesize that this rigid structure will provide a more accurate local temperature readout. Additionally, we would expect that the temperature values measured by the nanothermometers should be higher and more reliable and realistic, compared to those obtained from the strategy depicted in **Figure 1A**,

because of the closer proximity of the nanothermometers to the nanoheater.

To obtain this core-satellite nanocomposite, Au NRs coated with mesoporous silica (AuNR@mSiO_2) are used as seeds onto which Nd^{3+}-doped LaOCl nanoparticles[17] can be directly grown by thermal decomposition (**Figure 2A**). A similar method has been reported for the attachment of iron oxide nanoparticles on AuNR@mSiO_2.[28] We selected gold nanorods with a longitudinal LSPR close to the absorption band of Nd^{3+} ions, so that the same laser line could be used to simultaneously activate light-to-heat conversion and excite Nd^{3+} emission – to measure local temperature *via* photoluminescence. The silica shell around the nanoheaters provides not only enhanced stability, but also the necessary separation between the nanoheater and the nanothermometer to avoid quenching effects. Literature reports indicate that a separation distance above 10 nm is required, so the use of thinner silica shells would affect negatively the Nd emission intensity.[29, 30] We focused on optimizing the performance of the hydrophobic nanomaterial, as a proof of concept, while other aspects such as water dispersibility, biocompatibility, and *in vitro* or *in vivo* hyperthermia experiments remain to be explored.

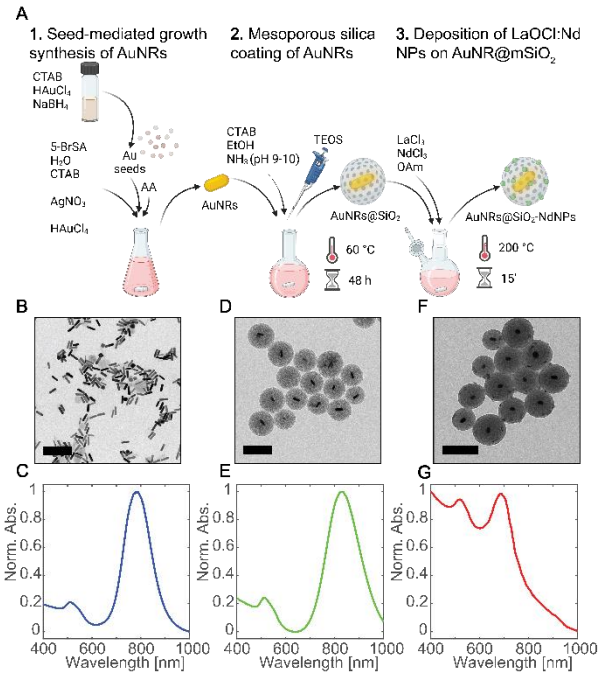

Figure 2. (A) Schematic view of the synthetic process used to produce AuNR@mSiO_2-NdNPs. TEM images (B,D,F) and normalized UV-visible spectra (C,E,G) of AuNRs (B,C), AuNR@SiO_2 (D,E), and AuNR@mSiO_2-LaOCl:Nd (F,G). Scale bars on TEM images represent 200 nm.

Materials and Methods

Chemicals. Lanthanum (III) chloride heptahydrate, 99.99% (Alfa Aesar), neodymium (III) chloride, anhydrous, 99.9% (Alfa Aesar) were stored under Ar atmosphere. Oleylamine (OAm, Sigma-Aldrich, 70%), oleic acid (OA, Alfa Aesar, 90%), ethanol (absolute), toluene (extra pure), and chloroform (Scharlau ACS basics, stabilized with ethanol) were stored in air prior to use. For the synthesis of gold nanorods 5-bromosalicylic acid (BrSal, technical grade, 90%), hydrogen tetrachloroaurate trihydrate ($HAuCl_4 \cdot 3H_2O$, ≥99.9%), hexadecyltrimethylammonium bromide (CTAB, ≥99%), silver nitrate ($AgNO_3$, ≥99.0%), L-ascorbic acid (AA ≥99%), and sodium borohydride ($NaBH_4$, 99%) were used. Milli-Q water was used in all experiments. For silica shell synthesis: Milli-Q water, ethanol, CTAB, NH_4OH, and tetraethyl orthosilicate (TEOS).

Synthesis of AuNRs. For the seed-mediated growth of gold nanorods with a LSPR at 800 nm, we followed the procedure described by Scarabelli *et al.*[10] Au seeds were prepared by mixing 4.7 mL of CTAB 0.1 M, 25 µL of 50 mM $HAuCl_4$ solution and 300 µL of 10 mM $NaBH_4$ at 27-30 °C, under vigorous stirring. Pre-reduction of Au (III) to Au (I) was then performed, by mixing 45 mg of BrSA, 25 mL of milli-Q water and 25 mL of 0.1 M CTAB, and 480 µL of 10 mM $AgNO_3$, to which 500 µL of 50 mM $HAuCl_4$ was then added. The reduction was monitored through the absorbance at 396 nm in the UV-visible spectrum of the solution and was stopped when the value reached 0.8. Immediately after, 130 µL of 100 mM AA and 80 µL of the seed solution were added. The mixture was left undisturbed for 4 hours. The obtained AuNRs were recovered by centrifugation at 7500-8000 rpm (9513-10824 ×g) and dispersed in water.

Synthesis of AuNRs@SiO_2. AuNRs were covered with a mesoporous silica shell with radially oriented channels, following the procedure described by Sanz-Ortiz *et al.*[31] Using this approach, silica was grown directly on gold nanorods with no need for any additional functionalization, as CTAB, used as capping surfactant for AuNRs, was also used as a template for the formation of porous shells. The shell thickness could be varied through the ratio between AuNRs and TEOS; to obtain a shell of approximately 50 nm, 5 mL of AuNR 5 mM and 200 µL of TEOS were used, for a total reaction volume of 250 mL.

In a rounded bottom flask, 170 mL of 6 mM CTAB solution and 75 mL of ethanol were mixed while stirring, and the temperature was maintained at 30 °C. Subsequently, 100-200 µL of 25 wt% ammonia solution was added to the mixture, to set a pH of 9-10, and successively 5 mL of 5 mM AuNR suspension was added. Finally, 200 µL of TEOS was added dropwise under vigorous stirring. The temperature of the reaction mixture was then increased to 60 °C and the product was recovered after 48 hours by centrifugation at 7000-7500 rpm (8287-9513 ×g) and washed with ethanol.

Synthesis of Nd-doped LaOCl nanoparticles. LaOCl:Nd nanoparticles were synthesized following the protocol described by Renero-Lecuna *et al.*,[17] to obtain a nominal 2 mol% Nd in the LaOCl crystal. The lanthanide precursor solution was prepared by mixing 0.5 mmol of $LaCl_3$ and

0.01 mol of $NdCl_3$, dissolved in 2 mL of methanol, and mixed with 20 mL of OAm. After degasification and water evaporation from the lanthanide precursors at 120 °C under vacuum, thermal decomposition was conducted by raising the temperature to 220 °C under Ar atmosphere for 1 hour. Finally, 2.5 mL of OA was added to detain the reaction. The purification of LaOCl:Nd nanoparticles was carried out by adding 5 mL of toluene to the solution followed by centrifugation at 9000 rpm (13699 ×g). The pellet was then redispersed in toluene and centrifuged again at 9000 rpm (13699 ×g), after the addition of few mL of ethanol to cause flocculation. Once the nanoparticles were recovered, they were dissolved in chloroform and could be kept in the refrigerator. The same synthesis was conducted with some variations,[17] by decreasing the reaction temperature to 200 °C rather than 220 °C, and the reaction time to 15 and 30 minutes instead of 1 hour.

Synthesis of AuNR@SiO_2-LaOCl:Nd nanocomposite. The AuNR@SiO_2-LaOCl:Nd nanocomposite was prepared using the milder version of LaOCl:Nd nanoparticle synthesis (200 °C, 15 minutes; see previous paragraph), using AuNR@SiO_2 as seeds. The amount of $LaCl_3$ (and Nd, always calculated as 2% of La) was reduced from 0.5 mM to 0.0625 mM, in the same reaction volume. The relative amounts of lanthanide precursors and AuNR@SiO_2 nanoparticles were optimized to reduce the potential homogeneous nucleation of LaOCl:Nd nanoparticles (outside the SiO_2 shell). For the first growth, 1.2 mL of the lanthanide precursors solution and 4 mL of the AuNR@SiO_2 dispersion in ethanol were added under vigorous stirring to 10 mL of OAm, at room temperature in a 2-neck rounded bottom flask. The temperature of the solution was then raised to 120 °C for degasification and finally heated up to 200 °C under Ar atmosphere, to induce thermal decomposition. After 15 minutes, 1 mL of OA was added to the reaction mixture and the temperature was decreased to room temperature by blowing air into the flask. Successively, the growth of LaOCl:Nd nanoparticles, with these new conditions, was repeated eight times. In particular, while for the first growth Au@SiO_2 nanoparticles were used as seeds, for the n^{th} growth the product of the $(n-1)^{th}$ growth step was used. For each growth step, the same amount (1.2 mL) of the lanthanide precursor solution was used. Purification of the final product was initially carried out by centrifugation at 8000 rpm (10824 ×g) for 15 minutes; then the precipitate was redispersed in chloroform and recovered at 2000-2500 rpm (676-1057 ×g), to separate it from LaOCl:Nd nanoparticles eventually nucleated in solution. The final pellet was redispersed in chloroform and kept in the refrigerator.

Transmission Electron Microscopy. For Transmission Electron Microscopy (TEM) and High-Resolution TEM [32] morphological characterization, the samples were diluted 2-10 times and deposited by dropcasting onto a carbon-coated copper TEM grid. The measurements were performed using a JEOL JEM-1400 PLUS TEM, operating at 120 kV. For Annular Dark-Field Scanning Transmission Electron Microscopy (ADF-STEM) imaging and Energy Dispersive X-ray Spectroscopy (EDS) measurements, an aberration corrected "cubed" Thermo Fisher Scientific Themis Z 60300 electron microscope operated at 300 kV was used. The probe convergence semi-angle was set to 21.5 mrad, and a camera length of 73 mm was used, which resulted in inner and outer collection semi-angles of 19 and 74 mrad, respectively. For EDS measurements, a Super-X detector (Oxford) was employed, and the maps were acquired for 15 min at a current of 50 pA.

Electron Tomography. For the electron tomography experiments, probe convergence semi angle of 21.5 mrad and a camera length of 73 mm were used. To obtain a 3D reconstruction of LaOCl:Nd NPs and SiO_2 shell, multimode tomography was used, as described by Sentosun *et al*.[32] This approach enables 3D reconstruction of materials containing low and high Z elements. Two ADF-STEM tilt series were acquired with inner and outer collection semi angles of 79 and 200 mrad, and 19 and 74 mrad, respectively. These tilt series were simultaneously recorded using a Fischione model 2020 tomography holder, between angles from -72° to 69° with a 3° increment. Inpainting was applied to the projection images with lower collection angles, replacing pixels corresponding to the AuNR with the surrounding SiO_2 texture. The processed tilt series were then reconstructed using the expectation-maximization (EM) algorithm implemented in the ASTRA tomography toolbox[33] and combined using the Amira software.

X-ray Photoelectron Spectroscopy (XPS). XPS experiments were performed on a SPECS Sage HR 100 spectrometer with a non-monochromatic X-ray source (Magnesium Kα line of 1253.6 eV energy and 252 W), placed perpendicular to the analyzer axis and calibrated using the $3d_{5/2}$ line of Ag with a full width at half maximum (FWHM) of 1.1 eV. The selected resolution for the spectra was 15 eV of Pass energy and 0.15 eV/step. All measurements were made in an ultra-high vacuum (UHV) chamber at a pressure around $8 \cdot 10^{-8}$ mbar. A flood gun was used for charge neutralization. After the first measurement, sputtering with an Argon ion gun was performed for 5 min at $8.9 \cdot 10^{-4}$ hPa and samples were measured again. Survey spectra were used for element quantification, while high-resolution spectra were used for fitting by CasaXPS. Calibration was performed using adventitious Carbon and fixing it at 284.8 eV. Peak attribution was done according to Moulder *et al*. unless specified.[34]

UV-Visible Spectroscopy. UV-visible optical extinction spectra were recorded using an Agilent 8453 UV-visible diode-array spectrophotometer.

Photoluminescence Spectroscopy. NIR photoluminescence (PL) measurements were performed using a homemade system. A diode fiber-coupled 808 nm laser (Lumics, LU808T040) was used to excite the colloidal dispersion through a collimated lens, with a spot size of 3 mm. The PL of the sample was collected through a fiber coupled

with a collimator lens and dispersed into an InGaAs spectrometer detector, operating between 900 and 1600 nm.

Photothermal Measurements

For photothermal (PT) heating experiments on AuNR@SiO_2-NdNPs, the colloidal dispersion was placed in a quartz cuvette and irradiated by an 808 nm laser at 33, 37, 40, 43, 46, or 49 W/cm^2. A FLIR A35 thermal camera was directed towards the top of the sample holder (cuvette), and the surface temperature in correspondence to the laser spot was monitored throughout the experiment. After the laser was turned on at the chosen laser power density and focused on the sample, the temperature was allowed to stabilize for at least 5 minutes, until reaching a plateau where the temperature increase did not exceed 0.5 °C for over a minute. When these conditions were achieved, the temperature value was reported, and PL measurements were used to determine the local temperature through Nd emission signals, using the nanothermometry method explained below. Each spectrum was collected with 2 seconds of acquisition time and averaged 50 times. The sample was allowed to cool down for 2 minutes and this procedure was systematically repeated for the different excitation powers.

Nanothermometry Measurements. Photoluminescence thermometry measurements were performed by using a ratiometric method, based on the Luminescence Intensity Ratio (LIR) of different peaks/emission bands, i.e. intraband or interband respectively, which are thermally linked, following the Boltzmann distribution function following equation: [35]

$$LIR(T) = \frac{I_{ii}}{I_i}(T) = B \cdot exp\left(-\frac{\Delta E}{k_B T}\right) \quad [1]$$

or in logarithmic form

$$lnLIR(T) = ln\left(\frac{I_{ii}}{I_i}\right)(T) = lnB - \frac{\Delta E}{k_B T} \quad [2]$$

where I_i and I_{ii} are integrated intensities of the peaks or bands used as thermal probes, *B* is the thermal calibration constant, *ΔE* the energy difference between levels from which the emission peaks originate, k_B the Boltzmann constant and *T* the local temperature expressed in K. The thermal calibration constant *B* in Equations [*1*] and [*2*] depends on several factors, among which the degeneracies of the involved states, their spontaneous emission rates, and their average spectral frequency, but also on how the environment and detector absorb or scatter at different wavelengths.[1,20].

For the thermal calibration of LaOCl:Nd^{3+} nanoparticles, we recorded emission spectra at various temperatures, within the range of 50 to 60 °C and determined fitting parameters for Eq. 2. When performing measurements using the nanocomposite, a recalibration of the B parameter was performed (Supporting Information, section 5) for a more accurate temperature determination.

Results and Discussion

Synthesis of nanocomposites

Multifunctional nanocomposites with hyperthermal and local temperature sensing capabilities were synthesized through a multi-step procedure, as schematically shown in **Figure 2A**. AuNRs were first synthesized using a standard seed-mediated growth method (Figure 2A, step 1).[10] The resulting cetyltrimethylammonium bromide (CTAB)-capped AuNRs had dimensions of 54.7 nm ± 5.0 nm × 14.9 nm ± 1.9 nm, as determined by transmission electron microscopy (TEM, **Figure 2B**), and a longitudinal LSPR band centered at 790 nm (**Figure 2C**). AuNRs were subsequently coated with a mesoporous silica shell through a modified Stöber synthesis, to produce AuNR@SiO_2 nanoparticles.[31] Briefly, a reaction mixture prepared by adding AuNRs, CTAB, and ethanol into water (see details in the Experimental section) was adjusted to pH 9 by controlled addition of aqueous ammonia, followed by dropwise addition of tetraethyl orthosilicate (TEOS) under vigorous stirring. After 48 hours of stirring at a constant temperature of 60 °C, the particles were recovered by centrifugation and redispersed in ethanol. Characterization by TEM (**Figure 2D**) and UV-visible spectroscopy (**Figure 2E**) revealed mesoporous silica shells with radially oriented channels (a higher resolution dark field scanning TEM image is shown in **Figure S1**). The average diameter of AuNR@SiO_2 nanoparticles was 161.2 nm ± 14.6 nm and the LSPR band was red shifted to 830 nm, as expected from an increase of the local refractive index around the AuNRs upon SiO_2 coating (**Figure 2C**, **E**).

The final step involved the sequential growth of Nd-doped LaOCl nanoparticles on the mesoporous silica shell surface, by adapting our previously reported protocol.[17] This step involves the addition of $LaCl_3$ and $NdCl_3$ to oleylamine (OAm), followed by increasing the reaction temperature to 220 °C for 1 hour, to decompose the lanthanide precursors and form LaOCl nanoparticles doped with Nd^{3+} ions. We chose here milder conditions, i.e. a shorter reaction time of 15 minutes and a lower reaction temperature of 200 °C, to prevent unwanted reshaping of the core AuNRs into Au nanospheres. We first proved that such milder conditions do not affect the properties of LaOCl:Nd^{3+} nanoparticles. The results for three different reaction conditions (1 hour at 220 °C; 30 minutes at 200 °C; 15 minutes at 200 °C) are summarized in **Figure S2A-F**, showing similar size distributions around 7.5 nm for all three samples, indicating that at 15 minutes, the synthesis is already completed. Optical characterization, upon photoexcitation at 808 nm, demonstrated the expected Nd^{3+} NIR luminescence bands at 900, 1060, and 1380 nm (**Figure S2G**), corresponding to the simplified Dieke's diagram (**Figure S2H**). Once the suitability of these conditions was established, we proceeded with the preparation of the

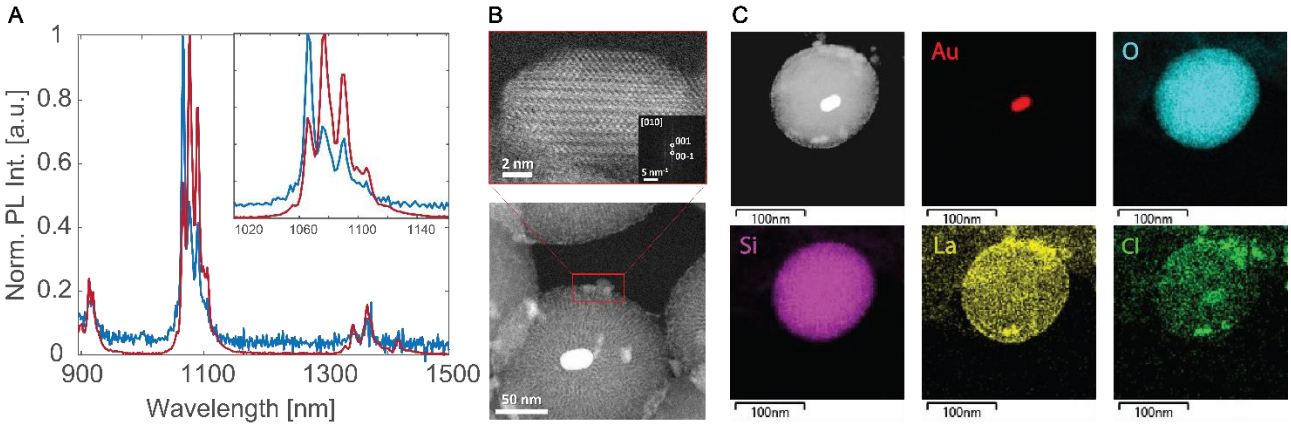

Figure 3. (A) Normalized photoluminescence spectra of LaOCl:Nd NPs (blue lines) and AuNR@mSiO_2-Nd nanocomposite particles (red lines), obtained by exciting the samples with an 808 nm laser. (B) High-resolution annular dark field-scanning TEM (ADF-STEM) image of a nanocomposite highlighting LaOCl:Nd NPs on the silica surface, and Fast Fourier Transform (FFT) (inset) matching with an (010) orientation. (C) ADF STEM and EDS elemental mapping for a nanocomposite particle.

nanocomposites, by adding AuNR@SiO_2 core-shell NPs to a reaction mixture containing $LaCl_3$ and $NdCl_3$ in OAm. The temperature was then increased to 200 °C and kept for 15 minutes, to grow LaOCl:Nd NPs on the AuNR@SiO_2 surface. The presence of these hydrophobic NPs on the SiO_2 surface accounted for the solubility of the nanocomposite in non-polar solvents such as chloroform. The LaOCl:Nd NP density on the AuNR@SiO_2 surface was gradually increased by sequential syntheses (up to 8x, see **Figure S3**). Both TEM analysis **(Figure 2F)** and changes in the UV-visible spectra – blue shifted LSPR peaks and modified relative intensities (**Figure 2G**) – for the final AuNR@SiO_2-LaOCl:Nd NPs, revealed partial reshaping of the central AuNRs, likely due to the high temperature used for the thermal decomposition reaction.[36,37] This effect is also visible in the TEM images of the intermediate growth products (**Figure S3B**). Upon increasing the temperature to 200 °C, which is required for the formation of LaOCl:Nd NPs, the AuNR aspect ratio decreased from an initial value of 2.8 ± 0.5 to 1.5 ± 0.3 in the final AuNR@SiO_2-LaOCl:Nd NPs (see statistical analysis in **Figure S3C**). As a result, a blueshift of the longitudinal LSPR band was observed from 830 to 670 nm (**Figure 2G**). Although not optimal, this shift did not create a significant issue because we were still able to reach the standard temperature in hyperthermia treatments (45°C) under 808 nm excitation wavelength, even under mild irradiation conditions (33 W/cm^2 laser power density). We also notice that the spectrum of hybrid NPs exhibits an increased scattering contribution, compared to AuNR@SiO_2 NPs. Since condensation of the SiO_2 shell was not detected (**Figure S3D**), this enhanced scattering may be due to the growth of LaOCl:NdNPs on the SiO_2 shell surface.

The results of the spectroscopic and morphological characterization of AuNR@SiO_2-LaOCl:Nd NPs are summarized in **Figure 3**. By comparing the normalized luminescence spectrum of a dispersion of AuNR@SiO_2-LaOCl:Nd NPs in chloroform (**Figure 3**A, red line), to that of LaOCl:Nd NPs in the same solvent (**Figure 3**A, blue line), we could readily assign the Nd^{3+} $^4F_{3/2} \rightarrow {}^4I_{13/2}$, $^4F_{3/2} \rightarrow {}^4I_{11/2}$, and $^4F_{3/2} \rightarrow {}^4I_{9/2}$ main transitions to the peaks centered at 900, 1060, and 1380 nm, respectively. Even though all bands were distinguishable from the background, the signal-to-noise ratio was strongly reduced because the concentration of luminescent NPs in the dispersion was significantly lower for the nanocomposite, with a consequent decrease in intensity. However, the luminescence intensity depends not only on the number of emitting centers (which is difficult to quantify in the nanocomposite), but also on factors such as the intensity of the excitation source and the increased light scattering contribution. In the inset of **Figure 3A**, we can see an excellent agreement between the position of luminescence bands in LaOCl:Nd and AuNR@SiO_2-LaOCl:Nd NPs, which suggests that the energies of the electronic levels involved in these transitions are not affected by any potential interaction of LaOCl:Nd NPs with the silica shell.

This result supports the hypothesis that the same product was obtained through the thermal decomposition protocol, both in the presence and in the absence of AuNR@SiO_2. It is worth noting that the relative intensities of Stark levels in the band centered at 1060 nm (originated from the $^4F_{3/2} \rightarrow {}^4I_{11/2}$ transition) were different in the AuNR@SiO_2-NdNPs photoluminescence (PL) spectrum, compared to LaOCl:Nd NPs. This is because the PL in oleylamine (OAm)-capped LaOCl:Nd NPs is much more intense than that of AuNR@SiO_2-LaOCl:Nd NPs, and the overlap of the Raman peak of $CHCl_3$, the solvent in which they are dispersed after synthesis, is therefore visible only in the latter case. The Raman spectrum of chloroform is characterized by a peak centered at 1067 nm when the excitation wavelength is 808 nm, corresponding to a Raman shift of 3004 cm^{-1}, as shown in **Figure S4.** The overlap between the emission from Nd^{3+} and the Raman scattering of chloroform is not apparent in the spectrum of LaOCl:Nd NPs, which is dominated by the strong PL intensity.

Morphological characterization of AuNR@SiO_2-LaOCl:Nd NPs was carried out by annular dark field scanning TEM

(ADF-STEM) of representative composite NPs (**Figure 3B**). The different elements present in the sample could be distinguished by their different contrast (a brighter Au core embedded in a lighter silica shell with radial pores and small nanocrystals deposited on the shell surface). A higher magnification image of such nanocrystals in the upper panel shows an elongated rod-like shape, with dimensions around 15 nm. By analyzing several images, we estimate the presence of around 12-15 NdNPs per nanocomposite. Moreover, high-resolution ADF-STEM images and FFT analyses from different LaOCl:Nd NPs (**Figures 3B** and **S5**), reveal that the crystalline structure matches with the expected tetragonal P4/nmm space group: 129.[38] **Figure 3**C shows X-ray energy dispersion spectroscopy (EDS) mapping for a single AuNR@SiO_2-LaOCl:Nd particle, with elemental maps for Au, O, Si, La, and Cl. The elemental distribution confirms the presence of Nd doped LaOCl NPs that partly cover the surface of silica coated gold nanorods. The EDS analysis of an AuNR@SiO_2-LaOCl:Nd NP is compared to that for AuNR@SiO_2 in **Figure S6**. Additionally, the 3D structure for several particles was analyzed by electron tomography (see a representative reconstruction in Supplementary **Video S1**), providing evidence that LaOCl:Nd NPs typically sit on the outer silica surface, but occasionally penetrate slightly through the shell porosity (see orthoslices in **Figure S7** and **Video S1**). Additionally, X-ray photoelectron spectroscopy (XPS) was performed on both LaOCl:Nd (**Figure S8A**) and AuNR@SiO_2-LaOCl:Nd NPs (**Figure S8B**). We could readily identify La $3d_{5/2}$ peaks at 834.7 and 838.6 eV for LaOCl:Nd, with a peak splitting of 4.1 eV, and at 836.0 and 839.4 eV, with a peak splitting of 3.4 eV for the nanocomposite. This result supports the growth of the nanothermometers on the SiO_2 outer shell of the nanocomposite. La 4p and Cl 2p peaks were also present in both XPS spectra, as shown in **Figures S8C** and **S8D**, respectively.

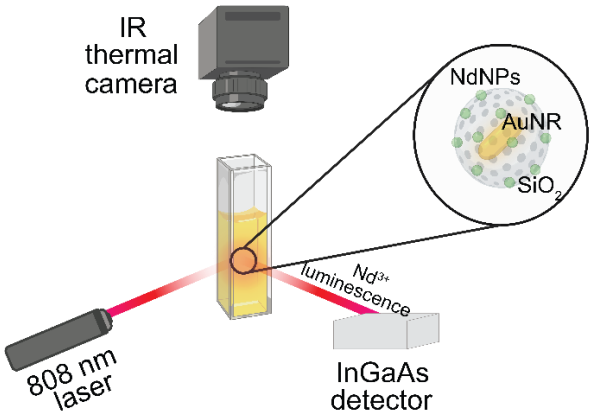

Figure 4. Description of the setup used for photothermal heating experiments. An 808 nm laser was used to induce heat release from AuNRs and temperature changes were detected by both a thermal camera and the photoluminescence of nanothermometers (LaOCl:Nd NPs) within the nanocomposite

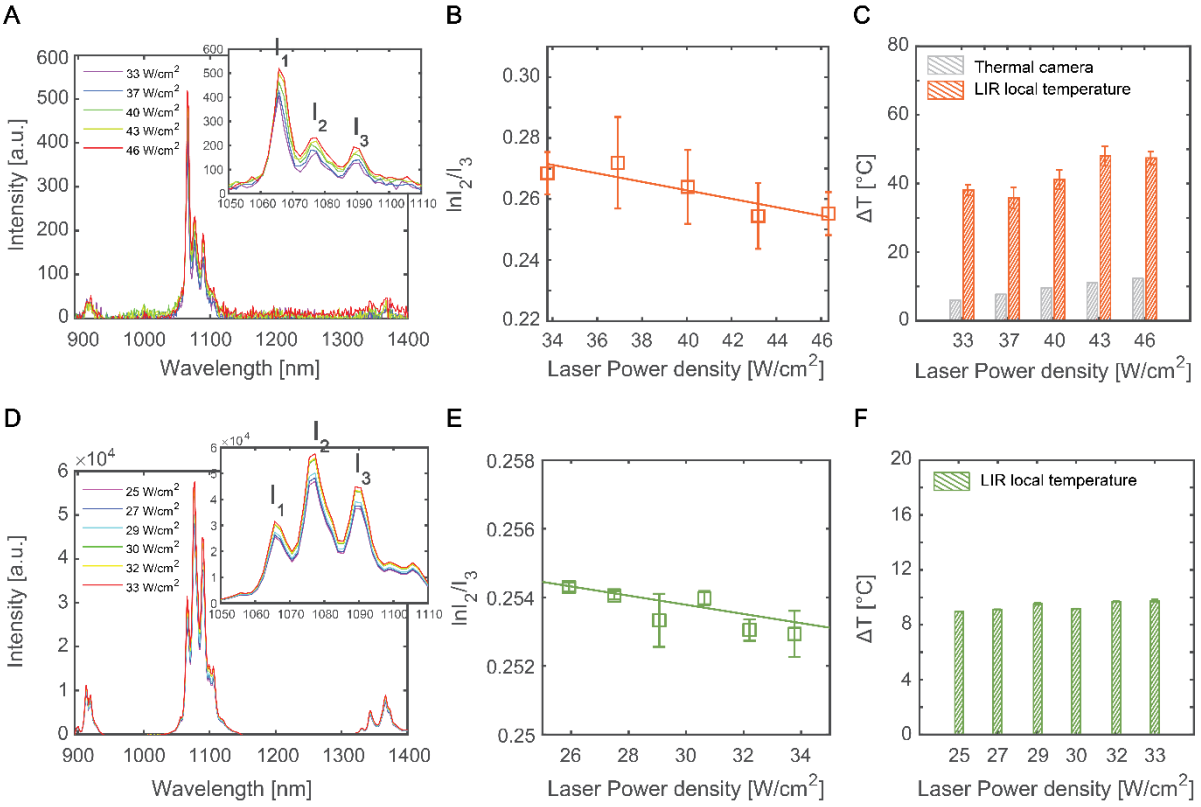

Figure 5. Photoluminescence spectra collected at different power densities of 808 nm laser irradiation (A,D), logarithm of the LIRs (average value ± standard deviation of five measurements) (B,E), and temperature increments (ΔT±δT) (C,F), resulting from photothermal heating experiments on AuNR@SiO_2-Nd NPs (A-B-C) and LaOCl:Nd NPs (D-E-F).

Local temperature monitoring during PT heating

The photothermal performance of AuNR@SiO_2-LaOCl:Nd NPs was investigated by irradiating the sample with an 808 nm laser, which was expected to induce light-to heat conversion by AuNRs and excite luminescence emission from Nd^{3+} ions. The laser irradiation setup (**Figure 4**) additionally included a thermal camera, placed on top, to detect (surface) temperature changes over time. The AuNR@SiO_2-LaOCl:Nd NPs dispersion was irradiated for at least 5 minutes, until the temperature, measured by a thermal camera, stabilized (i.e. the increase of *T* is less than 0.5 °C in 1 minute). Once a plateau temperature was reached, five emission spectra were collected, as shown in **Figure 5**A, for different laser power densities (33, 37, 40, 43, 46, and 49 W/cm^2, common literature values for PT range from 1 to 100 mW/cm^2 using CW lasers for sample excitation).[5] To detect the temperature increment near the AuNRs, the emission band corresponding to the $^4F_{3/2} \rightarrow {}^4I_{11/2}$ transition, which splits into Stark levels as a consequence of the crystal field effect, was used for intraband nanothermometry. These levels are thermally coupled, so that their population ratio depends on temperature and can be used to monitor local temperature through the corresponding luminescence intensity ratio (LIR) of the correspondent bands through **Equation 1** (Experimental section).

The luminescence spectra reported in **Figure 5A** and **Figure 5D** can be normalized to peak intensity $\boldsymbol{I_1}$ or $\boldsymbol{I_2}$ and temperature variation effects can be determined through the variation of peak intensity $\boldsymbol{I_3}$ (**Figure 5A** and **D** inset). As the first peak overlaps with the Raman scattering peak of the solvent, I_2 was chosen as the reference peak for nanothermometry. From each spectrum, the $\frac{\boldsymbol{I_2}}{\boldsymbol{I_3}}$ ratio was calculated, and the average logarithm of LIR was determined for each value of the power density, together with the standard deviation obtained from five repeated measurements (**Figure 5B**). As described in detail in the Experimental section, a calibration procedure was performed to determine the local temperature, presented in **Figure 5C** as $\Delta\boldsymbol{T} \pm \boldsymbol{\delta T}$, where $\Delta\boldsymbol{T}$ is the difference between the average final value (t=5 minutes) and the initial temperature (t=0, 20°C) ± the uncertainty derived from the standard deviation of the LIRs ($\boldsymbol{\delta T} = \frac{\boldsymbol{\delta lnLIR}}{\boldsymbol{lnLIR}} \cdot \boldsymbol{T}$). Besides, the local temperature determined with the LIR thermometry was compared to the temperature measured with the thermal camera. As expected, lower temperature increments $\Delta\boldsymbol{T}$ were detected by the thermal camera, which is measuring the average temperature of the colloidal dispersion (see comparison in **Figure 5C**) compared with those determined from the luminescence of the nanothermometers, pointing out the ability to measure the local temperature of our nanocomposites of the, since the nanothermometers are placed at an average distance of 80 nm away from the nanoheater.

The LaOCl:NdNP nanothermometers were able to measure a large temperature increment, as close as 80 nm from the AuNR in the core, demonstrating the localized high light-to-heat conversion efficiency. The use of an 808 nm laser allows to maximize the absorption by Nd^{3+} ions, and thus the luminescence intensity used for nanothermometry, while keeping a sufficiently high absorption by AuNRs to generate the temperature increase. In the present work, the mismatched plasmon resonance with the laser wavelength is favorable with respect to avoiding excessive heating in the environment around AuNRs, thereby preventing further AuNR reshaping. Also, no damage is expected to occur to the nanocomposites after the irradiation at different laser power densities since no changes in PL intensity nor spectral shape is reported during the irradiation time to heat up the sample (**Figure S9**).

Given the well-known ability of LaOCl:NdNPs alone to produce heat upon NIR photoexcitation,[39,40] we also conducted a photothermal heating control experiment on a colloidal suspension of LaOCl:Nd NPs in chloroform. The corresponding luminescence spectra, logarithm of $\frac{\boldsymbol{I_2}}{\boldsymbol{I_3}}$ LIR and temperature increment $\Delta\boldsymbol{T}$ with respect to room temperature (20 °C) are displayed in **Figure 5D-F**, as a function of photoexcitation power density. The same photothermal heating conditions as for AuNR@SiO_2-NdNPs were reproduced, irradiating the sample with an 808 nm laser, and waiting for 5 minutes prior to acquisition of the PL spectra. Interestingly, the thermal camera could detect not any temperature increment. However, a rather low local temperature increase could be recorded, ranging from 8.9 to 9.7 °C using the nanothermometers. The weak light-to-heat photothermal efficiency of NdNPs alone was in agreement with the existing literature, indicating a proportionality between the heat produced by the Nd-doped nanoparticles and their Nd^{3+} doping concentration (in our case the doping concentration was maintained low, at nominal ~2%).[17, 39] Therefore, the low doping concentration of Nd^{3+} ions in the nanothermometers together with the small number of NdNPs in the nanocomposite makes the heat produced by the nanothermometers negligible, not affecting the final temperature measurements

Conclusions

In this work it has been demonstrated that a multifunctional AuNR@SiO_2-LaOCl:Nd NPs nanomaterial could be used as a multifunctional material for hyperthermia treatments and also as temperature sensor, as the excitation laser wavelength for Nd^{3+} emission is at 808 nm, falling into the I BW, and its emission, used for thermometry, falls into the II BW. The combination of nanoheaters (AuNRs) and nanothermometers (NdNPs) within a single structure, which has obvious advantages in real in vivo experiments (with respect to the use of the two features in two individual species), was achieved. The Nd^{3+} emission

bands resulting from the photoexcitation of the hybrid AuNR@SiO_2-LaOCl:Nd NPs with the 808 nm laser could be exploited to determine the temperature increase due to the heat released by AuNR. The hybrid NPs have an adequate heating performance, at low nanoparticle concentration and moderate irradiation power, for their application in photothermal therapy. Indeed, even at the lowest laser power used in heating experiments, the temperature detected by the nanothermometers was enough to raise the surrounding temperature more than 35°C.

The optimal condition for achieving high luminescence intensity and the generation of a sufficient amount of localized heat was found to be the resonance of the laser wavelength with the Nd^{3+} ions absorption band in our host matrix (LaOCl)[17] enabling accurate local temperature determination. Besides, the nearly off-resonance of the laser wavelength with the longitudinal plasmon band of the AuNR avoids undesired uncontrolled heating in the surrounding area of the AuNRs.

Acknowledgements

L.L.L.-M. acknowledges financial support by the Spanish Agencia Estatal de Investigación and FEDER (PID2023-151281OB-I00), S.K. acknowledges the Flemish Fund for Scientific Research (FWO Vlaanderen) through a PhD research grant (Project numbers: 1181122N & 1181124N) and the European Research Council (CoG 815128, REALNANO).

Associated Content

Supporting Information

Additional experimental data, including TEM, HAADF, and elemental mapping images, XPS spectra as well as size analysis of the nanoparticles and nanocomposites.

Author Information

Corresponding Authors

Carlos Renero-Lecuna − CINBIO, University of Vigo, 36310 Vigo, Spain
orcid.org/0000-0002-3160-1795;
Email: carlos.renero@uvigo.gal

Luis M. Liz-Marzán − CIC biomaGUNE, Basque Research and Technology Alliance (BRTA), 20014 Donostia-SanSebastián, Spain; Ikerbasque, BasqueFoundation for Science, 48009 Bilbao, Spain; Centro de Investigación Biomédica en Red,Bioingeniería, Biomateriales y Nanomedicina (CIBER-BBN),20014 Donostia-San Sebastián, Spain; Cinbio, University of Vigo, 36310 Vigo, Spain
orcid.org/0000-0002-6647-1353;
Email: llizmarzan@cicbiomagune.es

Author Contributions

The manuscript was written through contributions of all authors. All authors have given approval to the final version of the manuscript.

References

1 Quintanilla, M., Henriksen-Lacey, M., Renero-Lecuna C., Liz-Marzán, K. M., Challenges for Optical Nanothermometry in Biological Environments**.** *Chem. Soc. Rev.* **2022**, *51*, 4223–4242.

2 Carey M. P., Burish, T. G., Etiology and Treatment of the Psychological Side Effects Associated with Cancer Chemotherapy: A Critical Review and Discussion. *Psychol. Bull.* **1988**, *104*, 307–325.

3 Johnson, J. E., Nail, L. M., Lauver, D., King, K. B., Keys, H., Reducing the Negative Impact of Radiation Therapy on Functional Status**.** *Cancer* **1988**, *61*, 46–51.

4 de la Encarnación, C., Jimenez de Aberasturi, D., Liz-Marzán, L. M., Multifunctional Plasmonic-Magnetic Nanoparticles for Bioimaging and Hyperthermia. *Adv. Drug Delivery Rev.* **2022**, *189*, 114484.

5 Jaque, D., Maestro, L. M., del Rosal, B., Haro-Gonzalez, P., Benayas, A., Plaza, J. L., Rodríguez, E. M., Solé, J. G., Nanoparticles for Photothermal Therapies. *Nanoscale* **2014**, *6*, 9494–9530.

6 Espinosa, A., Kolosnjaj-Tabi, J., Abou-Hassan, A., Plan Sangnier, A., Curcio, A., Silva, A. K. A., Di Corato, R., Neveu, S., Pellegrino, T., Liz-Marzán, L. M., Wilhelm, C., Magnetic (Hyper)Thermia or Photothermia? Progressive Comparison of Iron Oxide and Gold Nanoparticles Heating in Water, in Cells, and In Vivo. *Adv. Funct. Mater.* **2018**, *28*, 1803660.

7 Espinosa, A., Reguera, J., Curcio, A., Muñoz-Noval, A., Kuttner, C., Van de Walle, A., Liz-Marzán, L. M. et al., Janus Magnetic-Plasmonic Nanoparticles for Magnetically Guided and Thermally Activated Cancer Therapy. *Small* **2020**, *16*, 1904960.

8 Hemmer, E., Benayas, A., Légaré, F., Vetrone, F., Exploiting the Biological Windows: Current Perspectives on Fluorescent Bioprobes Emitting above 1000 nm. *Nanoscale Horiz.* **2016**, *1*, 168–184.

9 Skripka, A., Benayas, A., Marin, R., Canton, P., Hemmer E., Vetrone, F., Double Rare-Earth Nanothermometer in Aqueous Media: Opening the Third Optical Transparency Window to Temperature Sensing. *Nanoscale* **2017**, *9*, 3079–3085.

10 Scarabelli, L., Sánchez-Iglesias, A., Pérez-Juste, J., Liz-Marzán, L. M., A "Tips and Tricks" Practical Guide to the Synthesis of Gold Nanorods. *J. Phys. Chem. Lett.* **2015**, *6*, 4270–4279.

11 Sánchez-Iglesias, A., Jenkinson, K., Bals, S., Liz-Marzán, L. M., Kinetic Regulation of the Synthesis of Pentatwinned Gold Nanorods below Room Temperature. *J. Phys. Chem. C* **2021**, *125*, 23937–23944.

12 Scarabelli, L., Grzelczak, M., Liz-Marzán, L. M., Tuning Gold Nanorod Synthesis through Prereduction with Salicylic Acid. *Chem. Mater.*, **2013**, *25*, 4232–4238.

13 Grzelczak, M., Sánchez-Iglesias, A., Rodríguez-González, B., Alvarez-Puebla, R., Pérez-Juste, J., Liz-Marzán, L. M., Influence of Iodide Ions on the Growth of Gold Nanorods: Tuning Tip Curvature and Surface Plasmon Resonance. *Adv. Funct. Mater.* **2008**, *18*, 3780–3786.

14 Okabe, K., Inada, N., Gota, C., Harada, Y., Funatsu, T., Uchiyama, S., Intracellular Temperature Mapping with a Fluorescent Polymeric Thermometer and Fluorescence Lifetime Imaging Microscopy. *Nature Comm.* **2012**, *3*, 9.

15 Nexha, A., Carvajal, J. J., Pujol, M. C., Díaz, F., Aguiló, M., Lanthanide Doped Luminescence Nanothermometers in the Biological Windows: Strategies and Applications. *Nanoscale* **2021**, *13*, 7913–7987.

16 Dramićanin, M. D., Sensing Temperature via Downshifting Emissions of Lanthanide-Doped Metal Oxides and Salts. A Review. *Methods Appl. Fluoresc.* **2016**, *4*, 042001.
17 Renero-Lecuna, C., Herrero, A., Jimenez de Aberasturi, D., Martínez-Flórez, M., Valiente, R., Mychinko, M., Bals, S., Liz-Marzán, L. M., Nd^{3+}-Doped Lanthanum Oxychloride Nanocrystals as Nanothermometers. *J. Phys. Chem. C* **2021**, *125*, 19887–19896.
18 Deng Z. S., Liu, J., Mathematical Modeling of Temperature Mapping over Skin Surface and its Implementation in Thermal Disease Diagnostics. *Comput. Biol. Med.* **2004**, 34, 495–521.
19 Batal, M. A., Mearawi, G., Conversion of Absorbed Light Energy into Diffusive Thermal Energy in Biological Tissue. *Energy Procedia* **2012**, *19*, 158–166.
20 Quintanilla, M., Zhang, Y., Liz-Marzán, L. M., Subtissue Plasmonic Heating Monitored with CaF_2:Nd^{3+},Y^{3+} Nanothermometers in the Second Biological Window. *Chem. Mater.* **2018**, *30*, 2819–2828.
21 Carrasco, E., del Rosal, B., Sanz-Rodríguez, F., de la Fuente, A. J., Gonzalez, P. H., Rocha, U., Kumar, K. U., Jacinto, C., Solé J. G., Jaque, D., Intratumoral Thermal Reading During Photo-Thermal Therapy by Multifunctional Fluorescent Nanoparticles. *Adv. Funct. Mater.* **2015**, *25*, 615–626.
22 Quintanilla, M., García, I., de Lázaro, I., García-Alvarez, R., Henriksen-Lacey, M., Vranic, S., Kostarelos, K., Liz-Marzán, L. M., Thermal Monitoring During Photothermia: Hybrid Probes for Simultaneous Plasmonic Heating and Near-Infrared Optical Nanothermometry. *Theranostics* **2019**, *9*, 7298–7312.
23 Nigoghossian, K., Ouellet, S., Plain, J., Messaddeq, Y., Boudreau, D., Ribeiro, S. J. L., Upconversion Nanoparticle-Decorated Gold Nanoshells for Near-Infrared Induced Heating and Thermometry . *J. Mater. Chem. B* **2017**, *5*, 7109–7117.
24 Debasu, M. L., Ananias, D., Pastoriza-Santos, I., Liz-Marzán, L. M., Rocha, J., Carlos, L. D., All-In-One Optical Heater-Thermometer Nanoplatform Operative From 300 to 2000 K Based on Er^{3+} Emission and Blackbody Radiation. *Adv. Mater.* **2013**, *25*, 4868–4874.
25 Rocha, U., Hu, J., Rodríguez, E. M., Vanetsev, A. S., Rähn, M., Sammelselg, V., Orlovskii, Y. V., Solé, J. G., Jaque, D., Ortgies, D. H., Subtissue Imaging and Thermal Monitoring of Gold Nanorods through Joined Encapsulation with Nd-Doped Infrared-Emitting Nanoparticles. *Small* **2016**, *12*, 5394–5400.
26 Zhang, J., Cheng, X., Zhang, H., Zheng, J., Wang, J., Plasmon-Controlled Selective Emission Enhancement of Eu3+ with (Au Core)@(Y(V,P)O4:Eu) Nanostructures. *ACS Nano* **2023**, *17*, 10546–10559.
27 Lin, X., Kong, M., Wu, N., Gu, Y., Qiu, X., Chen, X., Li, Z., Feng, W., Li, F., Measurement of Temperature Distribution at the Nanoscale with Luminescent Probes Based on Lanthanide Nanoparticles and Quantum Dots. *Appl. Mater. Interfaces* **2020**, *12*, 52393–52401.
28 de la Encarnación, C., Jungwirth, F., Vila-Liarte, D., Renero-Lecuna, C., Kavak, S., Orue, I., Wilhelm, C., Bals, S., Henriksen-Lacey, M., de Aberasturi, D, J. et al., Hybrid Core–Shell Nanoparticles for Cell-Specific Magnetic Separation and Photothermal Heating. *J. Mater. Chem. B* **2023**, *11*, 5574–5585.
29 Ma, X.; Fletcher, K.; Kipp, T.; Grzelczak, M. P.; Wang, Z.; Guerrero-Martínez, A.; Pastoriza-Santos, I.; Kornowski, A.; Liz-Marzán, L. M.; Mews, A. Photoluminescence of Individual Au/CdSe Nanocrystal Complexes with Variable Interparticle Distances. *J. Phys. Chem. Lett.* **2011**, *2* (19), 2466–2471.
30 Gueroui, Z.; Libchaber, A. Single-Molecule Measurements of Gold-Quenched Quantum Dots. *Phys. Rev. Lett.* **2004**, *93* (16), 166108.
31 Sanz-Ortiz, M. N., Sentosun, K., Bals, S., Liz-Marzán, L. M., Templated Growth of Surface Enhanced Raman Scattering-Active Branched Gold Nanoparticles within Radial Mesoporous Silica Shells. *ACS Nano*, **2015**, 9, 10489–10497.
32 Sentosun, K., Sanz Ortiz, M. N., Batenburg, K. J., Liz-Marzán, L. M., Bals, S., Combination of HAADF-STEM and ADF-STEM Tomography for Core–Shell Hybrid Materials. *Particle & Particle Syst. Charact.* **2015**, *32*, 1063–1067.
33 van Aarle, W. Palenstijn, W. J., De Beenhouwer, J., Altantzis, T., Bals, S., Batenburg, K. J., Sijbers, J., The ASTRA Toolbox: A Platform for Advanced Algorithm Development in Electron Tomography. *Ultramicroscopy* **2015**, *157*, 35–47.
34 Moulder, J., Stickle, W. Sobol, W., Bomben, K. D., in: Chastain, J., Ed., Handbook of X-Ray Photoelectron Spectroscopy: A Reference Book of Standard Spectra for Identification and Interpretation of XPS Data, **1992** Perkin-Elmer Corporation, Waltham.
35 Jaque, D., Vetrone, F., Luminescence Nanothermometry. *Nanoscale* **2012**, *4*, 4301–4326.
36 Petrova, H., Perez-Juste, J., Pastoriza-Santos, I., Hartland, G. V., Liz-Marzán, L. M., Mulvaney, P., On the Temperature Stability of Gold Nanorods: Comparison between Thermal and Ultrafast Laser-Induced Heating. *Phys. Chem. Chem. Phys.* **2006**, *8,* 814–821.
37 Mohamed, M. B., Ismail, K. Z., Link, S., El-Sayed, M. A., Thermal Reshaping of Gold Nanorods in Micelles. *J. Phys. Chem. B* **1998**, *102*, 9370–9374.
38 Maslen, E. N., Streltsov, V. A., Streltsova, N. R., Ishizawa, N. Synchrotron X-ray Electron Density in the Layered LaOCl Structure. *Acta Cryst.* **1996**, *B52*, 576-579.
39 Rocha, U., Jacinto da Silva, C., Ferreira Silva, W., Guedes, I., Benayas, A., Martínez Maestro, L., Acosta Elias, M., Bovero, E., van Veggel, F. C. J. M., García Solé J. A. et al., Subtissue Thermal Sensing Based on Neodymium-Doped LaF3 Nanoparticles. *ACS Nano* **2013**, *7*, 1188–1199.
40 Marciniak, L., Pilch, A., Arabasz, S., Jin, D., Bednarkiewicz, A., Heterogeneously Nd^{3+} Doped Single Nanoparticles for NIR-Induced Heat Conversion, Luminescence, and Thermometry. *Nanoscale* **2017**, *9*, 8288–8297.

Graphic for Table of Contents only